Parametric study of anodic microstructures to cell performance of planar solid oxide fuel cell using measured porous transport properties

C.M. Huang [a], S.S. Shy [a,*], C.W. Chien [a], C.H. Lee [b]

[a] *Department of Mechanical Engineering, National Central University, 300 Jhong-da Road, Jhong-li 32001, Taiwan*
[b] *Institute of Nuclear Energy Research, Lung-tan, Tao-yuan 32546, Taiwan*

ABSTRACT

This study reports effects of porosity (ε), permeability (k) and tortuosity (τ) of anodic microstructures to peak power density (PPD) of a single-unit planar anode-supported SOFC based on 3D electrochemical flow models using measured porous transport properties. Applying particle image velocimetry, a transparent porous rib-channel with different ε is applied to measure an effective viscosity (μ_e) in the Brinkman equation commonly used to predict flow properties in porous electrodes. It is found that, contrary to the popular scenario, μ_e is not equal to the fluid viscosity (μ_f), but it is several orders in magnitude smaller than μ_f resulting in more than 10% difference on values of PPD. Numerical analyses show: (1) while keeping k and τ fixed with ε varying from 0.2 to 0.6, the highest PPD occurs at $\varepsilon = 0.3$ where the corresponding triple-phase-boundary length is a maximum; (2) PPD increases slightly with k when $k \leq 10^{-11}$ m^2 due to the diffusion limitation in anode; and (3) PPD decreases with τ when $\tau > 1.5$ due to the accumulation of non-depleted products. Hence, a combination of $\varepsilon = 0.3$, $k = 10^{-11}$ m^2, and $\tau = 1.5$ is suggested for achieving higher cell performance of planar SOFC.

© 2009 Elsevier B.V. All rights reserved.

1. Introduction

There is great interest in using the anode-supported solid oxide fuel cell (SOFC), because its thin electrolyte may signify it can generate electricity at reduced temperature ranging from 600 °C to 800 °C. In this temperature range, various low-cost materials can be applied to the cell and its auxiliary components, and as such, the influences of thermal cycles and thermal stresses to the cell's longevity may be mitigated [1]. On the other hand, when thick anodic electrodes are used, it is difficult to supply enough fuel to the reaction site commonly known as the triple-phase-boundary (TPB) [2]. Clearly, there is a need to carefully deal with the cell concentration polarization problem by the investigation of effects of anodic microstructure properties including such as porosity (ε), permeability (k) and tortuosity (τ) to cell performance, so that the anode-supported SOFC can be operated more properly at reduced temperatures. This motivates the present work.

Recently, many geometrical and numerical models have been developed to predict optimal electrodes' microstructures in attempt to enhance the cell performance of SOFCs. For instances, Deng and Petric [3] proposed a geometrical model to maximize the TPB length of the electrodes when both pore and grain sizes of 1 μm

with $\varepsilon = 0.3$ were used. Ni et al. [4] developed an electrochemical model based on the Bulter–Volmer equation, Fick's law and Ohm's law to study the influence of electrodes' microstructures to the cell performance. They found that the cell power can be maximized when the electrodes with a pore size of 3 μm and $\varepsilon = 0.4$ were used. Various numerical models were also developed to investigate the effect of the electrode's thickness to the cell performance of anode-supported SOFCs [5–7]. Though considerable progress has been made in understanding the influence of anodic microstructures to cell performance of planar SOFC, the actual transport phenomena occurring between flow distributors and porous electrodes which are crucial to the concentration polarization still remain unclear.

For planar anode-supported SOFCs, the momentum transfer in porous rib-channels of flow distributors features the supply of fuel and oxidant to the electrodes and thus has great influence on heat and species transports. In order to predict correctly the cell performance, proper flow models with accurate boundary conditions at the porous interface of rib-channels are required. Fig. 1 shows a typical variation of velocity profiles in a rib-channel across the anode. In it there are three different flow regions: (1) a free flow region with a nearly parabolic velocity profile which is governed by the second-order Navier–Stokes (N–S) equations, (2) a transitional region where the flow velocity decreases drastically until it reaches the Darcy's velocity, and (3) a porous region where the flow velocity is almost constant and is governed by the first-order Darcy's law [8]. Obviously, flow velocities and shear stresses in the transitional region cannot be matched by the second-order N–S equations
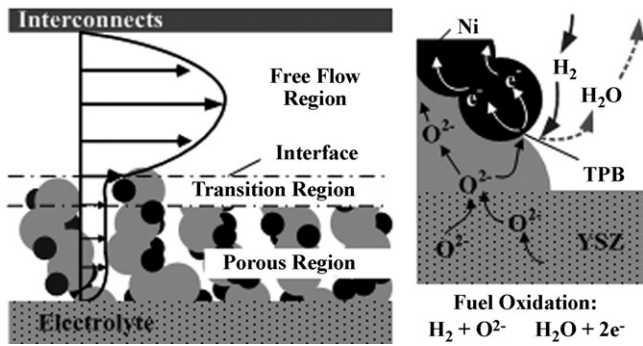
Fig. 1. Left: schematic velocity profiles across an anodic porous rib-channel between interconnect and electrolyte of a planar SOFC including three different flow regions. Right: a cartoon showing the fuel oxidation process occurred around the triple-phase-boundary (TPB).

Table 1
Material properties of various porous media used in this study.

Porous media	ε	$k^{0.5}$ (mm)	τ
Al$_2$O$_3$	0.04	1.1×10^{-4}	1.85
ZrO$_2$	0.17	3.87×10^{-4}	1.73
Ni-mesh	0.43	2.74×10^{-3}	1.48

and the first-order Darcy's law. Therefore, various approaches have been taken into consideration to solve such matching problem in numerical simulations, of which we introduce two most commonly used equations. The first equation was proposed by Brinkman [9] in a form of

$$\nabla p = -\left(\frac{\mu_f}{k}\right) U + \mu_e \nabla^2 U, \qquad (1)$$

where p, μ_f, μ_e, k, and U were the pressure, the fluid dynamic viscosity, the effective viscosity, the permeability, and the flow velocity. Eq. (1) is an extension of the Darcy's law with an additional second-order body force term ($\mu_e \nabla^2 U$), where μ_e acts as a fitting parameter. The second equation proposed by Beavers and Joseph [10] (hereafter refer to B&J) was a semi-empirical slip boundary condition at the porous interface indicating the strain rate just on the top of the porous interface,

$$\frac{du}{dy}|_{y=0^+} = \frac{\alpha}{\sqrt{k}}(U_s - U_D), \qquad (2)$$

where U_s is the free fluid velocity at the interface (the slip velocity), U_D is the Darcy's velocity, α is a slip coefficient, and k is the permeability of the porous medium. Since U_D is much smaller than U_s, Eq. (2) may be simplified to

$$\alpha = \dot{\gamma}\frac{\sqrt{k}}{U_s}, \qquad (3)$$

where $\dot{\gamma} = du/dy|_{y=0^+}$. It should be noted that the slip velocities obtained from the Brinkman equation and the B&J boundary condition are equivalent when $\alpha = (\mu_e/\mu_f)^{0.5}$, as confirmed by Neal and Nader [11]. Values of α may vary from 0.1 to 4 depending on the properties of porous media [10]. Moreover, an important experimental finding by Givler and Altobellic [12] showed that μ_e can be equal to μ_f ($\alpha = 1$) only when $\varepsilon > 0.9$ in porous flows. Without

the consideration of this experimental evidence, all current available numerical studies in modeling the momentum transport for SOFCs, see Refs. [13–16] among many others, all assumed $\mu_e = \mu_f$ in the Brinkman equation even though values of ε for SOFCs are within $0.2 < \varepsilon < 0.4$ which are much smaller than 0.9. To validate such assumption ($\mu_e = \mu_f$) used in the Brinkman equation, this study introduces an experimental platform for quantitative measurements of slip velocities at the porous interface with porosity closely matching that of SOFCs. Hence, the information on μ_e in the Brinkman equation (Eq. (1)) or α (Eq. (3)) may be obtained and the complex momentum transport across the porous interface of SOFCs may be investigated.

As the first objective, we measure slip velocities very near the porous interface using a prototypical porous rib-channel with values of ε ranging from 0 to 0.43 in a gaseous experimental platform using particle image velocimetry (PIV) and thus values of μ_e may be obtained. The second but equally important objective is to perform numerical sensitivity tests on effects of anodic microstructures to the cell performance. As shown on the right of Fig. 1, the main role of an anode is to provide the active sites for the electrochemical reaction, so that the oxide ions (O^{2-}) available from the electrolyte can react with the fuel at the TPB which locates around the contorted boundaries among the electrolyte, the electro-catalyst, and the gaseous fuel. This is why anodic microstructures are so crucial to the concentration polarization of the anode-supported SOFCs. As noted previously, quite a few studies are available for effects of anodic pore and grain sizes to the cell performance (e.g., Refs. [3–7]). However, very few studies are available for effects of k and τ to the cell performance. As pointed out by Koponen et al. [17], k represents the ability of the porous media to transmit fluid and τ indicates the shortest continuous flow paths between any two points within the pore space. An anode with proper values of k and τ can significantly improve the pathway of the gases within the porous electrodes which in turn can further increase the cell performance. Therefore, this study investigates numerically effects of ε, k, and τ to the cell performance of a single-unit planar anode-supported SOFC.

The following sections describe experimental methods used in this study, concerning measurements of gaseous velocity fields in porous rib-channels using PIV. A 3D electrochemical flow model for a single-unit planar anode-supported SOFC is then presented. Using the measured boundary conditions at the porous interface,
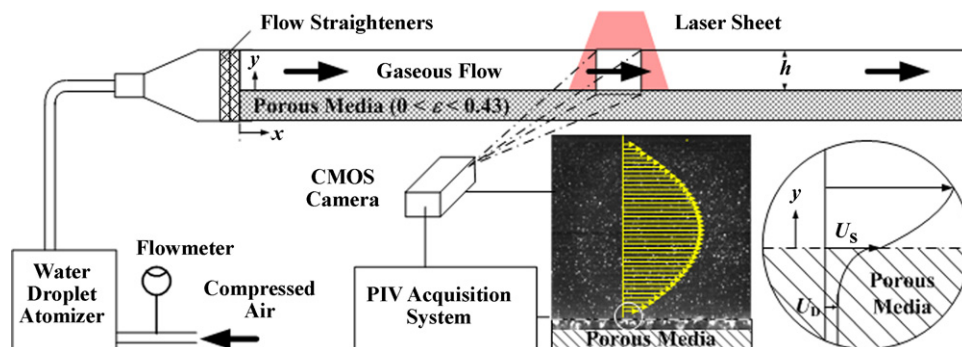

Fig. 2. The gaseous experimental platform for velocity measurements in a porous rib-channel using PIV, where U_s is the slip velocity at the porous interface and U_D is the Darcy velocity.

numerical simulations are performed and effects of various anodic microstructures to cell performance of the single-unit cell stack are discussed. Finally, conclusions are offered.

2. Experimental methods

Fig. 2 presents a gaseous platform consisting of a Plexiglas rib-channel with different porous materials, a TSI atomizer for seeding particles, and a PIV acquisition system. Three different porous media with different values of ε are applied, respectively, $\varepsilon = 0.04$ for aluminum oxide (Al_2O_3), $\varepsilon = 0.17$ for chromium oxide (ZrO_2), and $\varepsilon = 0.43$ for nickel mesh (Ni-mesh), which have microstructures similar to commonly used anodic materials for planar anode-supported SOFCs. These porous media are placed on the bottom of the rib-channel, so that velocity distributions in the porous rib-channel can be measured by PIV. In this study, a mercury intrusion porosimeter (Porous Materials, Inc., USA), is used to measure the porous properties (ε, k, and τ) of these three porous media, as listed in Table 1. The working fluid is air and its flow rate is controlled by a flowmeter mounted between the air bottle and the atomizer. A hydraulic Reynolds number ($Re = UD_h/\nu$) based on the hydraulic diameter of the rib-channel above the porous media is used to characterize the flow, where U is the mean velocity and ν is the kinematic viscosity of the working fluid. For simplicity, the present work considers a flow with fixed $Re = 100$ and measures corresponding velocity profiles in these porous rib-channels having different values of ε.

As can be also seen from Fig. 2, the coordinates, x and y, denote streamwise and transverse directions, with $x = 0$ at the inlet of the rib-channel and $y = 0$ at the porous interface. In order to perform PIV measurements, a small amount of tiny water droplets with a mean diameter of 3 μm issuing from the TSI atomizer was provided to the air flow. We applied 10 W diode laser with appropriate optical lenses to generate a laser sheet that cut the seeding flow in the middle of the rib-channel (see Fig. 2). A high-speed CMOS camera (512 × 512 pixels) positioned perpendicular to the plane of the laser sheet was used to record the evolution of the flow through the porous rib-channel using a frame rate of 2000 frames s^{-1} with a view field of 8.1 mm × 8.1 mm. All acquired images were then post-processed by a Matlab-based cross-correlation software using an interrogation window of 32 × 32 pixels with 75% overlapping. For detail treatment of PIV measurements, the reader is directed to Ref. [18]. An ensemble-average velocity profile in the porous rib-channel superimposed on an instantaneous flow image is also presented in Fig. 2, where the porous medium used is Ni-mesh. Due to the optical limitation, we cannot measure the velocity profiles inside the porous media using the current gaseous platform.

3. Numerical simulation

Fig. 3a shows a single planar SOFC stack consisting of a positive-electrode/electrolyte/negative-electrode (PEN) and a pair of interconnects with rib-channels to distribute fuel and air through the PEN. In order to correctly simulate various transport phenomena and electrochemical reactions occurring near the porous interface and the PEN, sufficiently dense computational grids must be applied to these regions. For simplicity, a 3D reacting model with one unit of the single-cell stack, as shown in Fig. 3b is considered, where the co-flow arrangement is applied for both anode and cathode, having a total grid-number of 250,000 for simulation (already very time-consuming). Using this 3D single-unit cell stack model, sensitive tests on effects of ε, k and τ to cell performance are performed, in which only one variable is changed at a time with the other variables fixed. The conservation equa-
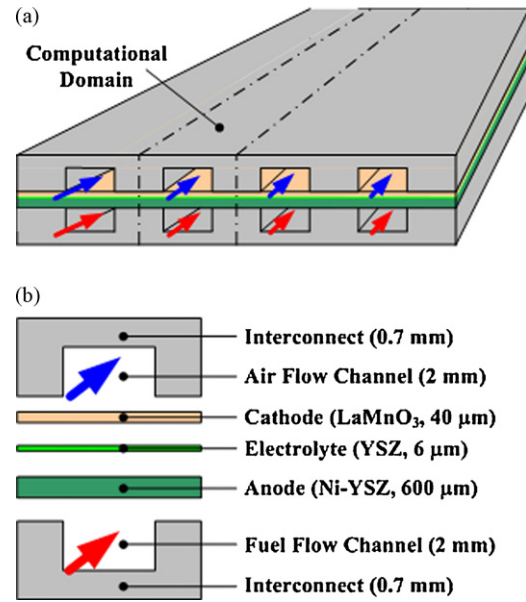

Fig. 3. (a) Schematic of a single anode-supported planar SOFC using the co-flow arrangement. (b) Same as (a), but for a single-unit cell used in a 3D reacting flow model.

tions of mass, momentum, energy, and species together with the fuel-reforming reactions and electrochemical reactions in the planar single-unit cell stack are solved using the CFD-RC package based on a finite volume approach with appropriate computational grids.

Since the simulations for both non-reacting and reacting flows are performed in a steady state condition, the mass continuity equation can be described by

$$\nabla \cdot (\varepsilon \rho \vec{U}) = S_m, \tag{4}$$

where ε is the porosity, ρ is the density of the multi-component gas mixture calculated by the ideal gas law, and S_m is a source term generated by chemical and electrochemical reactions. The laminar incompressible momentum equation can be written in a form of

$$\nabla \cdot (\varepsilon \rho \vec{U} \vec{U}) = -\varepsilon \nabla p - \frac{\varepsilon^2 \mu_f \vec{U}}{k} + \varepsilon \mu_e \nabla^2 \vec{U}, \tag{5}$$

where p is the pressure. The energy equation is

$$\nabla \cdot (\varepsilon \rho \vec{U} h_0) = \nabla \cdot \vec{q} + \varepsilon \bar{\bar{\delta}} \nabla \vec{U} + S_e \tag{6}$$

where h_0 is the enthalpy of the gases, $\vec{q}$ is the heat flux, and S_e is the heat source term from the heat transport and the species diffusion. The variations of thermal properties for both gases and solid materials with temperature are also considered in the simulation. The species conservation equation can be expressed

$$\nabla \cdot (\varepsilon \rho Y_i) = \nabla \cdot J_i + \omega_i, \tag{7}$$

where Y_i, J_i, and w_i are the mass fraction, the diffusion flux, and the production rate of the ith species in the gas phase, respectively. In this study, the transport properties, such as the species diffusivities are calculated using a sub-model based on the Stefan–Maxwell equation. Finally, a Bulter–Volmer equation is applied for the correlation between electrochemical reactions and current density in the catalytic layer, as shown below

$$j = j_0 \left[\exp\left(\frac{\lambda_a F}{RT}\right) \eta - \exp\left(\frac{\lambda_c F}{RT}\right) \eta \right] \prod_{i=1}^{N} [i]^{\beta_i}, \tag{8}$$

where λ_a and λ_c are the kinetic constants determined from the experimental Tafel slopes [19], j and j_0 are the current density and the reference current density at a known open circuit voltage, and F and R are the Faraday constant and the gas constant, respectively. The other parameters in Eq. (8) are the overpotential between the electronic and ionic phases (η), the interfacial concentration of ith species ($[i]$), the total number of reacting species (N), and the concentration exponents of the ith species (β_i), respectively.

In this study, fuels are syn-gases with 9.6% H_2, 26% CO, 21.6% CO_2, and 42.8% H_2O based on the mass fraction. The composition of air is 79% N_2 and 21% O_2. For the anode, hydrogen is oxidized via $H_2 + O^{2-} \rightarrow H_2O + 2e^-$. Simultaneously, the reduction of oxidant occurs at the cathode is via 0.5 $O_2 + 2e^- \rightarrow O^{2-}$. Since hydrogen can be reformed from carbon monoxide at high-temperature conditions, the water–gas-shift reaction, $CO + H_2O \rightarrow CO_2 + H_2$, is also included in both fuel channels and porous anode using a reaction rate described by the Arrhenius law [20]. For all electrochemical reacting flow simulations in this study, we keep Re fixed with $Re_{anode} = 100$ and $Re_{cathode} = 300$.

4. Results and discussion

4.1. Velocity distributions in a porous rib-channel

Fig. 4a presents four sets of normalized gaseous velocity distributions measured in a porous rectangular rib-channel with four different values of ε varying from 0 to 0.43 (different symbols) at $Re = 100$ using PIV, where $U_c(\varepsilon = 0)$ is the centerline velocity of the rib-channel at $\varepsilon = 0$ and h is the rib-channel height above the porous media. For clarity, only two sets of numerical data at $\varepsilon = 0$ and $\varepsilon = 0.43$ (dash lines) using the assumption of $\mu_e = \mu_f$ in the Brinkman equation are included in Fig. 4a for comparison. Since the present porous media are not optically accessed, PIV measurements can only be performed above the porous interface. Moreover, the image processing very near the porous interface ($y/h < 0.025$) may suffer higher experimental uncertainties due to the light scattering from the surface and thus PIV data below $y/h = 0.025$ will not be presented in Fig. 4a. For the case of $\varepsilon = 0$, numerical flow data are in a very good agreement with experimental PIV data. But for the case of $\varepsilon = 0.43$, numerical flow data close to the porous interface ($y/h < 0.1$) are found to be smaller than the available experimental data. This is because the assumption of $\mu_e = \mu_f$ is used in numerical flow simulations. Taking a close look at velocity profiles near the porous interface from Fig. 4a and b shows the same velocity data within $-0.1 \le y/h \le 0.1$ where $y/h = 0$ is the porous interface. To the first-order approximation, these three PIV data sets at three different values of ε (solid symbols) in Fig. 4b are linearly fitted with their fitting lines extending to the porous interface. This may allow us to estimate the slip velocities ($\hat{U}_{s,exp}$) (open symbols) and corresponding strain rates ($\dot{\gamma}$) at the porous interface. The difference of normalized slip velocities between experimental and numerical data, is $\Delta \hat{U}_s = \hat{U}_{s,exp} - \hat{U}_{s,num}$, as indicated in Fig. 4b. It is found that the higher the value of ε is, the higher the magnitude of $\Delta \hat{U}_s$ (see the inset in Fig. 4b). Applying Eq. (3), the effective viscosity (μ_e) can be estimated by $\mu_e = \mu_f \alpha^2$ [11]. As shown on the inset of Fig. 4b, μ_e is sensitive to ε for which the ratio of μ_e/μ_f increases from 10^{-4} to 4.9×10^{-3} when ε increases from 0.04 to 0.43. These results show that the assumption of $\mu_e = \mu_f$ commonly used in the Brinkman equation for numerical simulations of SOFCs cannot predict correctly the momentum transport in the porous media when $0 < \varepsilon \le 0.43$, because the actual slip velocities at the porous interface are underestimated.
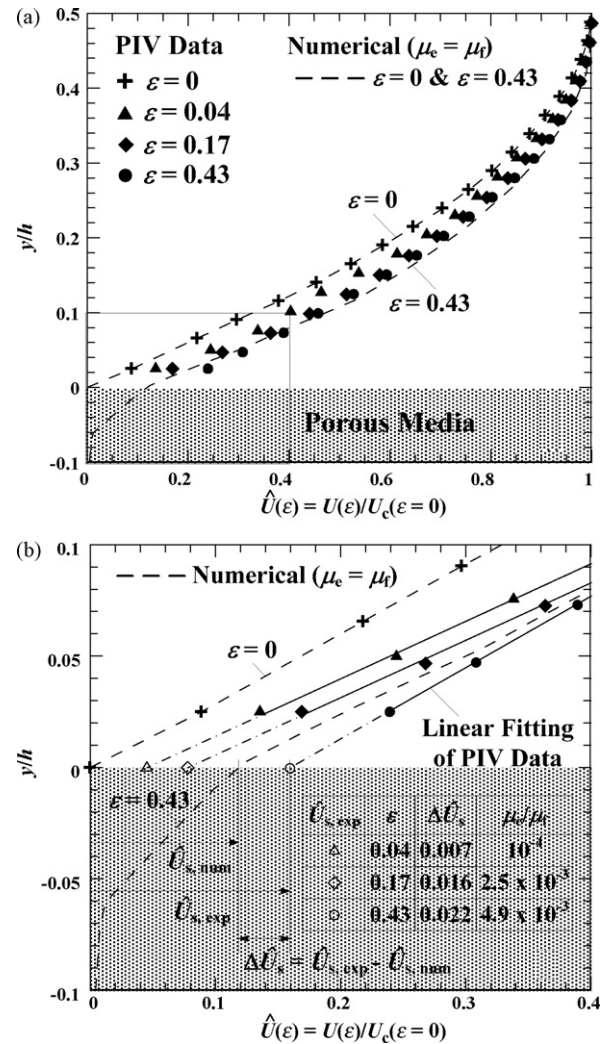

Fig. 4. (a) Four sets of normalized gaseous velocity profiles in a rectangular rib-channel with four different values of ε varying from 0 to 0.43 at $Re = 100$ measured by PIV. For clarity, only two sets of numerical data at $\varepsilon = 0$ and $\varepsilon = 0.43$ using the assumption of $\mu_e = \mu_f$ in the Brinkman equation are included for comparison. (b) Same data as (a), but only for velocity profiles near the porous interface showing the estimation of $\hat{U}_{s,exp}$ using the linear fitting. The inset table lists corresponding values of ε, $\Delta \hat{U}_s$, and μ_e/μ_f estimated from PIV data.

4.2. Effect of μ_e/μ_f on cell performance

So μ_e is not equivalent to μ_f and it is several orders in magnitude smaller than μ_f. It is thus important to know the influence of such difference between μ_e and μ_f in the Brinkman equation to the cell performance. Currently, this influence can be only studied by numerical simulations. Applying the same single-unit cell stack model described in Section 3 with two drastically different values of μ_e/μ_f while keeping all the other conditions fixed, Fig. 5 shows two data sets of corresponding voltage and power density as a function of current density, where the same values of $\varepsilon = 0.3$, $k = 10^{-11}$ m^2, $\tau = 1.5$, $Re_{anode} = 100$, and $Re_{cathode} = 300$ are used in the model. It is found that the value of peak power density (PPD = 531 mW cm^{-2}) occurring at 818 mA cm^{-2} for $\mu_e/\mu_f = 4.9 \times 10^{-3}$ is nearly 11% higher than that of $\mu_e/\mu_f = 1$ (PPD = 475 mW cm^{-2} at 731 mA cm^{-2}). Clearly, this increase in the value of PPD up to 11% indicates that the effect of μ_e/μ_f plays a role on the cell performance and thus cannot be neglected.

Since our experimental data reveal that the ratio of μ_e/μ_f varies with ε, we thus perform sensitivity analyses of the ratio of μ_e/μ_f to
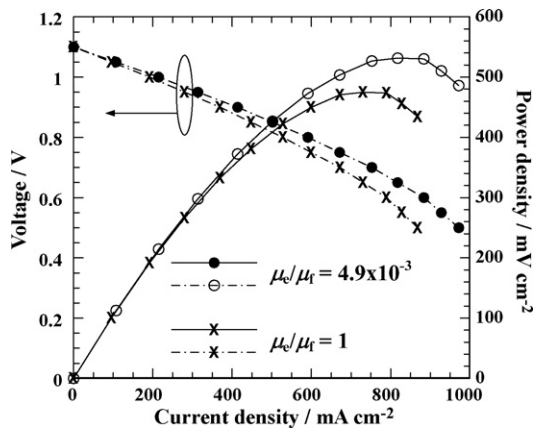
Fig. 5. Comparison of power-generating characteristics when two different values of μ_e/μ_f are used in the same single-unit cell stack model with fixed values of $\varepsilon = 0.3$, $k = 10^{-11}$ m², $\tau = 1.5$, $Re_{anode} = 100$, and $Re_{cathode} = 300$.

the peak power density of the single-unit cell stack at three different values of ε. These results are presented in Fig. 6 showing three points. First, for all three different values of ε, values of PPD increase from about 470 mW cm^{-2} to about 520 mW cm^{-2} when the ratio of μ_e/μ_f decreases from 1 to 0.1. Secondly, further decreasing of μ_e/μ_f from 0.1 to 0.01 results in only a little increase of PPD and then values of PPD remain constant when $\mu_e/\mu_f \leq 0.005$. Thirdly, values of PPD at $\varepsilon = 0.3$ are found to be higher than those at $\varepsilon = 0.2$ and at $\varepsilon = 0.4$ showing the effect of ε on the power density. These results may be understood from the governing equations used in numerical simulations. For instance, the additional second-order body force term $(\varepsilon \mu_e \nabla^2 \vec{U})$ in the Brinkman equation involving the effective viscosity which is the last term of Eq. (5) should act as a drag force imposed by the boundaries of the grains in porous electrodes. When the Brinkman equation with the assumption of $\mu_e/\mu_f = 1$ is used, such drag force as the resistance to flow will be overestimated resulting in a decrease of the amount of the reactant that could penetrate into the triple-phase-boundary (TPB) around the reaction sites. But when μ_e/μ_f is sufficiently small $(\mu_e/\mu_f < 0.01)$ as suggested by the present sensitivity analysis (Fig. 6), the drag force term, $\varepsilon \mu_e \nabla^2 \vec{U}$, becomes insignificant and the mass transport in porous electrodes should be dominated by the Knudsen diffusion and/or the molecular diffusion. This may explain why the value of PPD obtained at $\mu_e/\mu_f = 4.9 \times 10^{-3}$ can be 11% higher than that when using $\mu_e/\mu_f = 1$ (see Fig. 5).
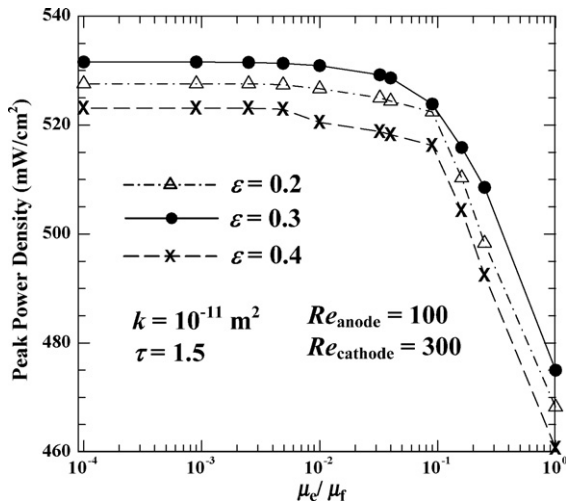

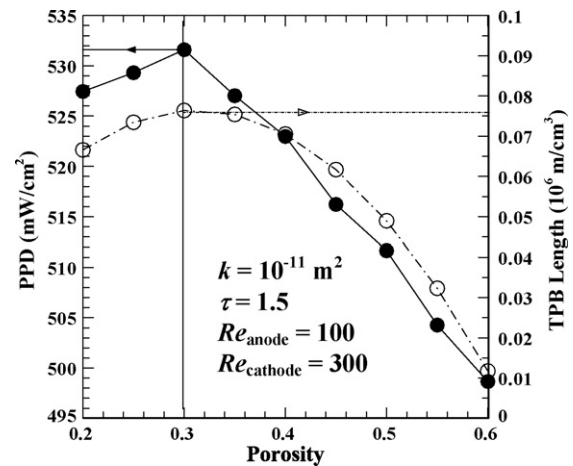**Fig. 6.** Variations of peak power density with μ_e/μ_f at three different values of ε.

Fig. 7. Peak power density and TPB length as a function of ε.

Can the present measured values of μ_e/μ_f be applicable when different anode materials and/or different cell configurations (anode-supported vs. electrolyte-supported or planar-type vs. tubular-type) are used? The answer is yes, because the present PIV measurements consider only fluid dynamics aspects for porous flows with an emphasis on the effect of porosity. Hence, the present PIV results should be valid even for real applications as long as the porosity of the material is fixed. However, real applications are very complex, because the electrochemical reactions might change the porosity of the electrodes. For instances, the chromium poisoning and the carbon deposition may reduce the porosity of electrodes. For cases with changing porosity, the present PIV data obtained at fixed values of porosity must be viewed with caution. In this study, we only consider constant values of porosity and thus we shall use measured transport properties, as shown on the inset table of Fig. 4, for further numerical studies.

4.3. Effects of ε, k and τ on cell performance

In attempt to predict an optimal combination of anodic microstructures for planar anode-supported SOFCs, we perform sensitivity tests on effects of ε, k, and τ to the cell performance using 3D single-unit cell stack model with measured porous transport properties. In it only one variable is changed at a time while keeping the other variables constant. At fixed values of $k = 10^{-11}$ m² and $\tau = 1.5$, Fig. 7 presents the effect of ε on the cell performance. It is found that the maximum PPD = 531 mW cm^{-2} occurs at $\varepsilon = 0.3$. Also plotted in Fig. 7 is the variation of the TPB length with ε, where the TPB length is calculated using the formula proposed by Deng and Petric [3]. As can be seen, the increasing and decreasing trends for both PPD and TPB length are essentially the same of which their maximum values all occur at $\varepsilon = 0.3$. On the one hand, it is known that smaller values of anodic ε may provide more reaction sites in anode which may result in higher values of PPD. On the other hand, too small anodic ε can reduce the mass transport rate due to the decrease of the Knudsen diffusion and the molecular diffusion in anode resulting in lower values of PPD. These two opposite effects may explain why the maximum values of PPD and TPB length occur at $\varepsilon = 0.3$.

Figs. 8 and 9 show the effect of k and the effect of τ on PPD, respectively, each including three different values of ε, where $Re_{anode} = 100$ and $Re_{cathode} = 300$ are used for both cases. At any given values of k and τ, values of PPD at $\varepsilon = 0.3$ are found to be larger than those at either $\varepsilon = 0.2$ or $\varepsilon = 0.4$, similar to the results of Figs. 6 and 7. Results from Fig. 8 show that values of PPD increase slightly with k when 10^{-12} m² < k < 10^{-11} m² and then little increase
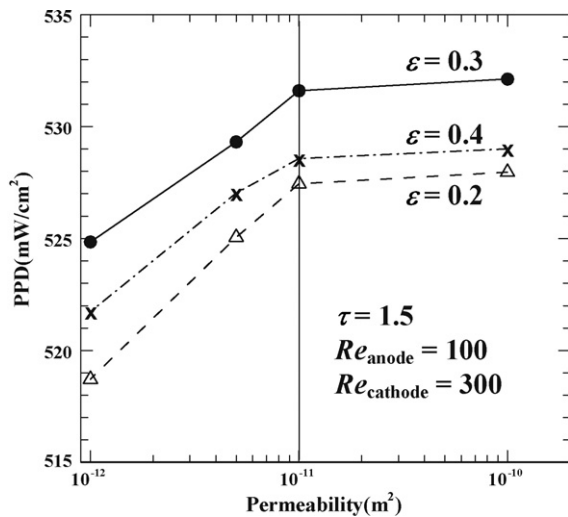
Fig. 8. Variations of peak power density with the anodic permeability at three different values of ε.
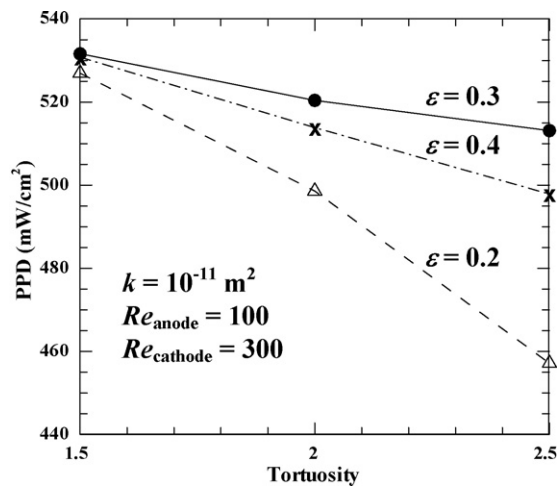

Fig. 9. Variations of peak power density with the anodic tortuosity at three different values of ε.

of PPD is found when 10^{-11} m$^2 < k < 10^{-10}$ m^2. Porous anodes with larger values of k may enhance the penetration of reactant to have a larger Darcy's velocity resulting in a higher PPD, but their mechanical strength is weakened. Since the TPB length and thus the effect of ε have much stronger influence on the cell performance (Fig. 7) than the effect of k, the appropriate value of $k \approx 10^{-11}$ m^2 is suggested for the anode-supported SOFCs. Concerning the effect τ, we found that values of PPD increase with decreasing τ. It is known that the ohmic polarization may be increased with increasing τ because of the increase of transport paths for ions and electrons in anode. Furthermore, the anode with larger values of τ would inhibit the exchange of H$_2$O and H$_2$ and thus increase the concentration polarization, suggesting that the value of τ for the anode should be as small as possible. But $\tau < 1.5$ is considered not practical for real anodic microstructures [2]. In addition, the effect of τ is more significant in the dense anode (smaller ε), as can be seen from Fig. 9, in which a 13% increase of PPD can be found when values of τ decrease from 2.5 to 1.5 with $\varepsilon = 0.2$ while only 3% increase of PPD is found at $\varepsilon = 0.3$. To this end, these results suggest that a combination of $\varepsilon = 0.3$, $k = 10^{-11}$ m^2, and $\tau = 1.5$ used in anodic microstructures can achieve the highest PPD.

5. Conclusions

This study aims to predict optimal anodic microstructures for planar anode-supported SOFCs using 3D electrochemical flow model with measured porous transport properties. Two key points are summarized below.

(1) A transparent porous rib-channel with different values of ε varying from 0 to 0.43 is applied to measure an effective viscosity (μ_e) in the Brinkman equation commonly used to predict flow properties in porous electrodes using PIV. It is found that, contrary to the popular scenario, μ_e is not equal to the fluid viscosity (μ_f), but it is several orders in magnitude smaller than μ_f which can result in more than 10% difference on the cell's power density.

(2) Numerical sensitivity analyses based on a single-unit cell stack model found that while keeping k and τ fixed with ε varying from 0.2 to 0.6, the highest PPD occurs at $\varepsilon = 0.3$ where the corresponding triple-phase-boundary length is a maximum. An optimal combination of $\varepsilon = 0.3$, $k = 10^{-11}$ m^2, and $\tau = 1.5$ for anodic microstructures is suggested to achieve higher cell performance.

These results should be useful for further improvement of the cell performance of planar SOFCs.

Acknowledgements

Appendix A. Supplementary data

Supplementary data associated with this article can be found, in the online version, at doi:10.1016/j.jpowsour.2009.10.048.

References

[1] S.C. Singhal, K. Kendall, High-temperature Solid Oxide Fuel Cells: Fundamentals, Design and Applications, Elsevier Ltd., Kidlington, 2003.
[2] A.V. Virkar, J. Chen, C.W. Tanner, J.W. Kim, Solid State Ionics 131 (2000) 189–198.
[3] X. Deng, A. Petric, J. Power Sources 140 (2005) 297–303.
[4] M. Ni, M.K.H. Leung, D.Y.C. Leung, Energy Convers. Manag. 48 (2007) 1525–1535.
[5] H. Fukunaga, M. Ihara, K. Sakaki, K. Yamada, Solid State Ionics 86–88 (1996) 1179–1185.
[6] E. Hernandez-Racheco, D. Singh, P.N. Hutton, N. Patel, M.D. Mann, J. Power Sources 138 (2004) 174–186.
[7] S.H. Chan, Z.T. Xia, J. Appl. Electrochem. 32 (2002) 339–347.
[8] J. Bear, Dynamics of Fluids in Porous Media, Dover Publications, New York, 1988.
[9] H.C. Brinkman, Appl. Sci. Res. A1 (1947) 27–34.
[10] G.S. Beavers, D.D. Joseph, J. Fluid Mech. 30 (1967) 197–207.
[11] G. Neal, W. Nader, J. Chem. Eng. 52 (1974) 475–478.
[12] R.C. Givler, S.A. Altobelli, J. Fluid Mech. 258 (1994) 355–370.
[13] P. Dokamaingam, S. Assabumrungrat, A. Soottitantawat, I. Sramala, N. Laosiripojana, Int. J. Hydrogen Energy 34 (2009) 410–421.
[14] D. Cui, L. Liu, Y. Dong, M. Cheng, J. Power Sources 174 (2007) 246–254.
[15] G. Wang, Y. Yang, H. Zhang, W. Xia, J. Power Sources 167 (2007) 398–405.
[16] C.M. Huang, S.S. Shy, C.H. Lee, J. Power Sources 183 (2008) 205–213.
[17] A. Koponen, M. Kataja, J. Timonen, Phys. Rev. E 54 (1996) 406–410.
[18] T.S. Yang, S.S. Shy, J. Fluid Mech. 526 (2005) 171–216.
[19] CFD-RC, CFD-ACE+ User Manual, CFD-RC, Huntsville, USA, 2003, http://www.cfdrc.com.
[20] J.M. Klein, Y. Bultel, S. Georges, M. Pons, Chem. Eng. Sci. 62 (2007) 1636–1649.